EARTH OBSERVATION AND GEOMATICS ENGINEERING
website: https://eoge.ut.ac.ir

Feasibility assessment of exploitation of distributed scatterers in InSAR stacks over pasture areas for different SAR satellite missions

Sami Samiei-Esfahany[1]*, Ramon Hanssen[2]

[1] School of Surveying and Geospatial Engineering, University of Tehran, Tehran, Iran
[2] Department of Geoscience and Remote Sensing, Delft University of Technology, Delft, the Netherlands

Article history:
Received: 7 March 2018, Received in revised form: 25 August 2018, Accepted: 2 September 2018

ABSTRACT

During the last decades, time-series interferometric synthetic aperture radar (InSAR) has emerged as a powerful technique to measure various surface deformation phenomena of the earth. Early generations of time-series InSAR methodologies, i.e. Persistent Scatterer Interferometry (PSI), focused on point targets, which are mainly man-made features with a high density in urban areas and associated infrastructure. Later, methodologies were introduced aiming to extract information from other targets known as distributed scatterers (DS), which are associated with ground resolution cells occurring mainly in rural areas. For some terrain types, such as agricultural terrain or pastures, the feasibility of DS-methodologies is not straightforward. In this paper, we investigate the feasibility of DS exploitation in pasture areas over a case study area over a solution salt mining-induced subsidence field in Veendam, the Netherlands. Based on the temporal coherence behavior of the DS-pixels in the pasture areas, we assess the feasibility of exploiting the DS-pixels by different satellite missions. The results show that assuming a three-year stack of data, the information content in DS-pixels from current C-band and X-band missions is not enough for the successful utilization of their entire time-series. However by using intermittent series, e.g., by processing individual coherent periods, the results indicate that DS-pixels can be exploited: based on the proposed decorrelation model, the short repeat times of Sentinel-1 (6 or 12 days) results in a sufficient number of coherent interferograms over each winter period, enabling DS exploitation even over agricultural and pasture areas.

KEYWORDS

InSAR
Temporal decorrelation
Radar interferometry
Distributed scatterers

1. Introduction

During the last decades, time-series interferometric synthetic aperture radar (InSAR) has emerged as a powerful technique to measure various surface deformation phenomena of the earth. Early generations of time-series InSAR methodologies, i.e. Persistent Scatterer Interferometry (PSI), focused on point targets, which are mainly man-made features with a high density in urban areas and associated infrastructure (Ferrettiet al., 2000; Ferretti et al., 2001; Adam et al., 2003; Werner et al., 2003; Hooper et al., 2004; Kampes, 2005; Costantini, et al., 2009; van Leijen, 2014). Later, methodologies were introduced aiming to extract information from other targets known as *distributed scatterers* (DS), which are associated with ground resolution cells occurring mainly in rural areas (Sandwell & Price, 1998; Wright et al., 2001; Berardino et al., 2002; Schmidt & Bürgmann, 2003; Lanari, et al., 2004; Hooper, 2008; Monti-Guarnieri & Tebaldini, 2008; Ferretti et al., 2011; Pepe et al.,

* Corresponding author
E-mail addresses: s.samieiesfahany@ut.ac.ir (S. Samiei-Esfahany), r.f.hanssen@tudelft.nl (R. Hanssen)

DOI: 10.22059/eoge.2018.267528.1032

2015; Fornaro et al., 2015; Cao et al., 2016; Samiei-Esfahany et al., 2016).

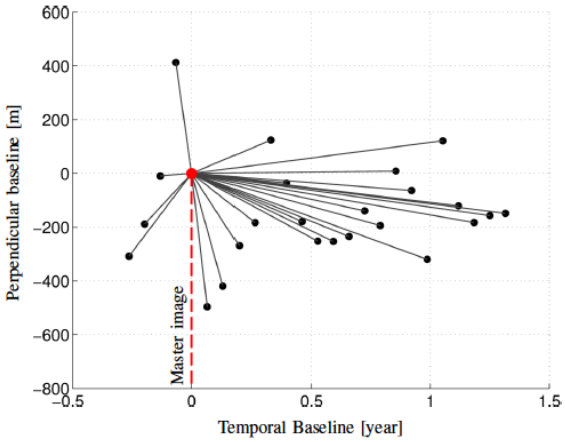

Figure 1. The baseline configuration of the used dataset, containing 25 radar images acquired between October 2011 and May 2013. The acquisition of 24 January 2012 has been used as an arbitrary master image.

Despite the potential value in methodologies exploiting DS, the feasibility of such methods for deformation monitoring over rural areas with a pasture and vegetation landscape, which has a high phase-decorrelation rate (Morishita & Hanssen, 2015), is still a pending question. One of the main limiting factors in exploitation of DS-pixels is temporal decorrelation. This effect is the result of variation in scattering phases between the two SAR acquisitions, due to the actual changes in the scattering characteristics of the elementary scatterers within a resolution cell. This could be either due to a change in the physical distribution of elementary scatterers (e.g. caused by soil weathering, anthropogenic activities, vegetation growth, and plant movements in the wind), or due to the variation in electrical properties of the scatterers (e.g. change in the dielectric constant of targets influenced by a variation in moisture content). The phase variation due to temporal decorrelation results in loss of coherence. High temporal coherence is common on surfaces without vegetation (e.g., arid areas, deserts, road and building surfaces). The lower extreme of temporal decorrelation is associated with water bodies where the scattering characteristics are changing rapidly within seconds.

Some recent studies have been reported a seasonally varying coherence behavior of DS-pixels in pasture fields, resulting in a different temporal-decorrelation rate between summer and winter periods, e.g. in Morishita and Hanssen (2015) and S. Samiei-Esfahany (2017). Our objective, in this paper, is to investigate the feasibility of DS exploitation in this kind of areas. To limit the scope, we chose a case study area over a solution salt mining-induced subsidence field in Veendam, the Netherlands. First, the feasibility of exploiting PS, DS, and their combination over pasture and agricultural landscapes is empirically assessed via an InSAR timeseries processing over the case study area. It is shown that, under the condition of using the entire time-series, agricultural and pasture areas show only limited improvement in point density compared to the results of PS-only processing. It is hypothesized that the low number of detected DS-pixel is due to the seasonal behavior of the temporal coherence, which causes an almost complete drop in coherence during summer periods, mainly as a result of tillage, crop growth and harvesting. Then, in the second phase of this study, based on the temporal coherence model of typical DS-pixels in the pasture areas, we theoretically assess the feasibility of exploiting DS-pixels by different satellite missions.

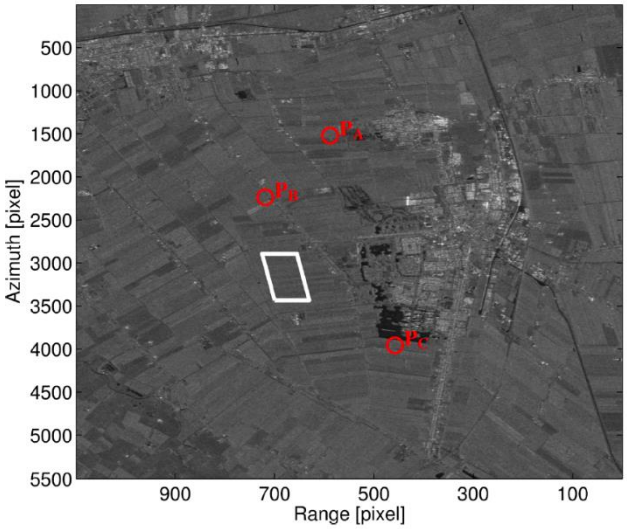

Figure 2. The location of three example coherence matrices of points P_A, P_B, and P_C in agricultural/pasture areas. The coherence matrices of these eight examples are shown/analyzed in fig. 3. The white box shows the location of a 1 km^2 area that has been used later for estimating the coherence matrix used for the temporal decorrelation modeling/validation in Section 4.

2. A Priori Analysis: coherence pattern and periodicity in temporal decorrelation

To evaluate the temporal decorrelation over pasture and agricultural areas, a test site around a salt mining area close to the city of Veendam in the north part of The Netherlands is chosen. A RadarSAT2 dataset containing 25 radar images acquired between October 2011 and May 2013 is used for the study. Figure 1 shows the baseline configuration of the used dataset, using the image of 24 January 2012 as an arbitrary master image. We estimated the coherence matrix at three different testing locations denoted by PA, PB, and PC in Figure 2. For coherence estimation, an adaptive brotherhood area is selected around each pixel based on the two-sample.

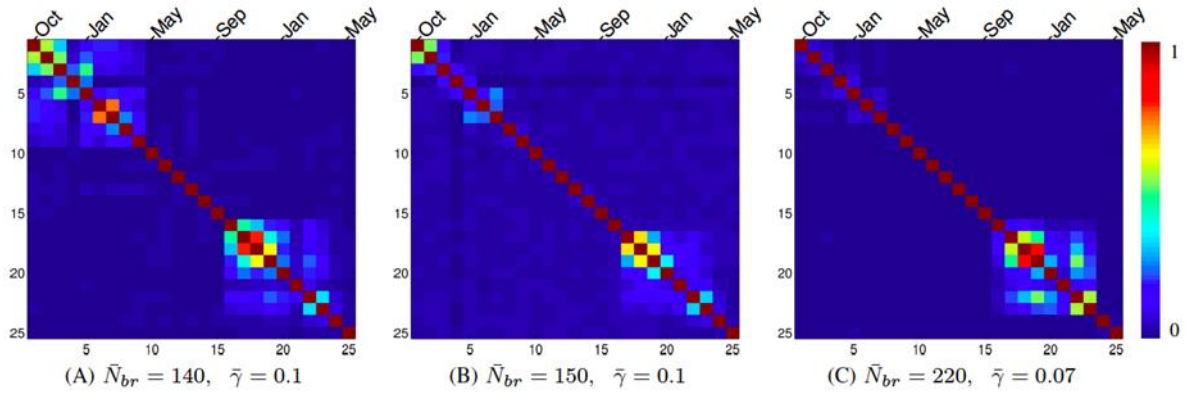

Figure.3 (A), (B), and (C) are three examples of coherence matrices in rural/pasture areas, cor*responding to the locations P_A, P_B, and P_C* in fig. 2. In the coherence matrices, the images are sorted based on the acquisition date (the months of acquisitions are indicated above the matrices). These matrices are the result of averaging coherence mat*rices of surrounding pixels. The* average number of brothers and mean coherence of averaged pixels is indicated by $\bar{N}_{br}$ *and* $\bar{\gamma}$ respectively.

The coherence matrices of the Figure.3 (A), (B), and (C) are three examples of coherence matrices in rural/pasture areas, corresponding to the locations P_A, P_B, and P_C in fig. 2. In the coherence matrices, the images are sorted based on the acquisition date (the months of acquisitions are indicated above the matrices). These matrices are the result of averaging coherence matrices of surrounding pixels. The average number of brothers and mean coherence of averaged pixels is indicated by $\bar{N}_{br}$ and $\bar{\gamma}$ respectively. Three testing locations are shown in Figure 3 A, B, and C respectively. To get more precise coherence estimation, the matrices presented here are the average of the estimated coherence matrices of the neighboring pixels in a 300 × 300 meter surrounding.

The first observation is that the interferograms with a short temporal-baseline show a relatively high coherence in the winter period (note that the images are sorted based on the acquisition date, so the close-to-diagonal elements represent interferograms with shorter temporal baselines.). In contrast, in the summer period (between May and October), the coherence values are almost zero even for consecutive acquisitions with a 24 days temporal baseline. These results indicate that the temporal decorrelation in these cases is faster in summer than in winter, possibly as a result of crop growth and tillage of agricultural lands during the summer period. For pasture areas in the Netherlands, it has been shown by Morishita and Hanssen (2015) that the coherence level of C-band interferograms with repeat intervals of 24-35 days (for RadarSAT2 and ERS/Envisat) is quite low. Even with a multilooking factor of L=200, the information content of such interferograms is not significant. In fact, due to the loss of coherence, the summer-acquisitions do not convey any useful information. The results of Figure 3 also reveal that, although the coherence level of short-baseline interferograms in winters is high, there is almost no coherence between two winter periods (as indicated by the low coherence values in the upper-right and the lower-left part of the coherence matrices).

It should be noted that, in algorithms that tries to exploit the entire timeseries of DS-pixels, it is important to have a connected coherent path through all the acquisitions of the dataset, via relatively high-coherence interferometric phases. The results of Figure 3 over agricultural/pasture areas around Veendam, show that the summer-acquisitions cause a disconnect path, and so the exploitation of these kinds of pixels in agricultural/pasture areas may not be feasible.

3. A posteriori analysis: combined PS-DS time-series processing

With "a-posteriori analysis" we mean the analysis of the results of applying ESM-phase estimation combined with a standard PSI processing to the RadarSAT2 stack over Veendam. We will compare the results of the combined PS-DS processing with the results obtained by standard PSI processing, and evaluate the density improvements over different landscapes.

3.1. Processing setting

We applied a two-step hybrid methodology similar to the *SqueeSAR* approach by (Ferretti et al., 2011). The flowchart of the algorithm is depicted in Figure 4. The particular settings that we used in each step are described in the following.

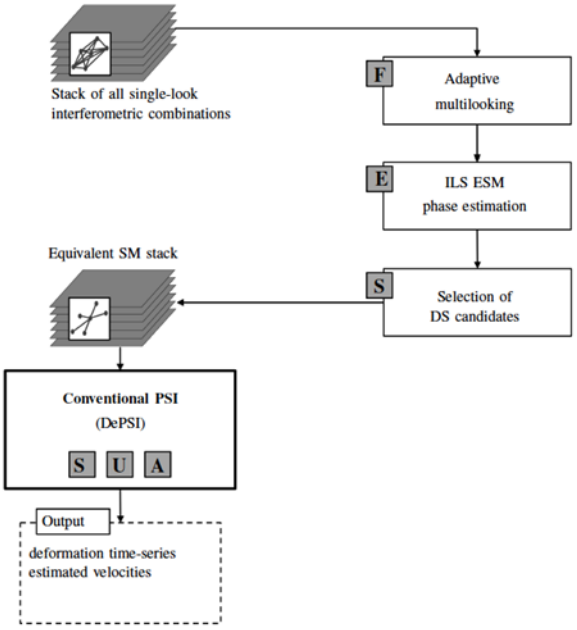

Figure.4 Generic flowchart of the hybrid methodology used for the Veendam case study. The processing steps are classified into the five basic Timeseries InSAR processing blocks (S: pixel selection, U: unwrapping, A: atmospheric-signal mitigation, F: filtering, and E: equivalent SM-phase estimation or phase linking.)

- **Adaptive multilooking:** The multilooked phases for each pixel are computed by spatial averaging over statistically homogeneous pixels (SHP) detected by the Kolmogorov-Smirnov test. The brother pixels are selected within a window of 25 × 25 pixels. In order to reduce the spatially variable signal within the multilooking areas, the topographic phase component is computed and subtracted from all the interferograms, using the SRTM digital elevation model.
- **ESM-phase estimation or phase linking:** After SHP selection and multilooking, we applied the ILS equivalent single-master (ESM) phase estimation (as proposed in S.Samiei-Esfahany (2016). using all the possible interferometric combinations. This step is applied on all the pixels in the case study area.
- **Selection of DS candidates:** After ESM-estimation, the posterior coherence factor (as introduced in Ferretti et al., (2011)) was estimated for each pixel. Pixels with a coherence factor larger than 0.4 and with more than 25 brothers were selected as potential DS. In order to make the final ESM-stack of interferograms, for the selected pixels, we replaced the phase of the original SM interferograms with the phase estimates of ILS ESM-phase estimation. By using the pixels with more than 25 brothers, the phase time-series of PS-pixels are not affected by ILS-phase estimation. In fact, in the new ESM-stack the PS-pixels get their original phase, whereas for the selected DS-pixels, the ESM-phases are used.
- **Conventional PSI processing:** For PSI processing, we used the *Delft implementation of persistent scatterer interferometry* (DePSI) (van Leijen, 2014).We made a modification to DePSI regarding the combined PS-DS processing by changing the initial PS-candidate selection method. The PS candidates were selected using the standard amplitude dispersion method, while the DS-candidates, which had been selected in the previous step, were added to the set of PS-candidates. The combined set of PS and DS pixels was processed by DePSI[1]. The final selection of coherent points (both PS and DS) was abstained by thresholding on the estimated *ensemble coherence* of the pixels. The threshold of 0.7 was used for the final selection. In addition, pixels with an absolute estimated velocity larger than 3 cm/year and an estimated height larger than 100 meter were selected as false-detections, and were removed from the final results.

In the next section, we analyze the final results obtained by applying the aforementioned algorithm.

3.2. Results

The results of applying the hybrid PS-DS processing on the Veendam case are shown in Figure 5. We applied both the standard DePSI processing with the original SM interferograms, and also with the estimated equivalent SM interferograms. The obtained velocity maps are presented in Figures 5A and 5B, respectively. The same processing setup has been used for both cases. Also, the density of detected PS/DS-pixels is shown in Figures CA and 5D. The results

[1] Specific settings of DePSI processing used in this study: a linear model and the bootstrapping approach have been used for temporal phase unwrapping, a Gaussian kernel with a length of one year has been used for atmosphere filtering, and the pixels associated with side-lobes of PS-pixels have been detected and removed before further processing (van Leijen 2014)}.

show a significant increase in the number of scatterers, especially in urban areas. Although the general density is also improved in the rural areas, most of the new detected DSs are in areas around buildings or on the roads. Only a very low number of DS-pixels is detected over agricultural fields or pasture areas. In fact, this low density was expected based on the a-priori analysis of the temporal-coherence behavior over agricultural/pasture landscapes (see section 2). In these areas, the coherence is almost entirely lost during the summer period, and the phase quality of DS-pixels in ESM-phase timeseries is not sufficient to detect these points as being persistent in the PSI processing.

Based on the land-use map of the area, we classified the detected PS/DS-pixels into two classes of urban/roads and agricultural/pasture. While the number of points in urban/road areas increased from 12594 to 144815 (almost 12 times larger), it improved from 1709 to 11003 pixels in the agricultural/pasture areas (i.e., four times more). As stated in section 2, the limited relative improvement in point density for agriculture regions is mainly due to the fact that the entire timeseries is used, rather than focusing on coherent subsets in time. Another important remark is that the phases, and consequently all other phase-derived estimates (e.g. velocities), of adjacent DS-pixels have some degree of correlation. This is due to the overlap between DS brotherhood areas that have been used in the adaptive multilooking. Therefore, the effective density-improvement is less than what we observe just by counting the detected DS-pixels independently and assuming no correlation between them.

Nevertheless the main message of these results is that the added value of DS processing, in areas with similar landscape, is mainly in urbanized areas. The DS-pixels over agricultural and pasture regions do not generally have sufficiently consistent phase quality in order to be successfully exploited over multiple years in the PSI processing. Based on the a-priori analysis of section 2 over these areas, the main reason for this low phase quality is the seasonal behavior of the temporal coherence, which causes almost zero coherence during summer periods.

4. Temporal coherence model for pastures

In order to evaluate the feasibility of exploitation of DS-pixels and to study the effect of different factors—such as satellite revisit time, radar wavelength, or multilooking factor—on DS phase quality, we require an analytical model for temporal decorrelation capable of describing the observed seasonal decorrelation pattern. We use the periodic model as presented by S. Samiei-Esfahany (2017):

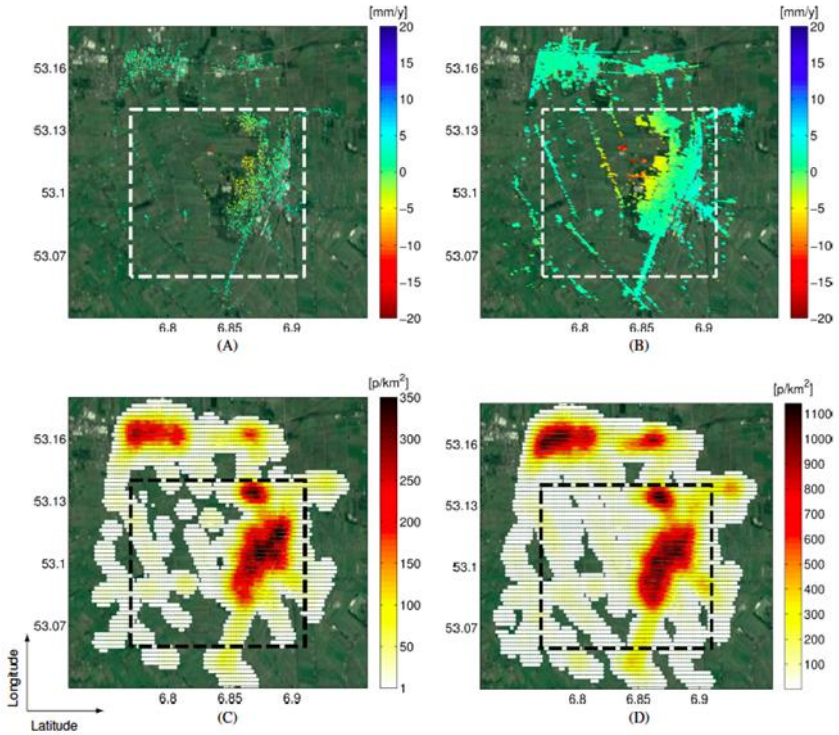

Figure 5. Predicted coherence matrices for studying the feasibility of DS exploitation for different radar satellite missions over agricultural/pasture areas, based on the estimated and assumed model parameters in Table 1. Three years of data are assumed resulting in different number of images for each mission (due to their different repeat interval).

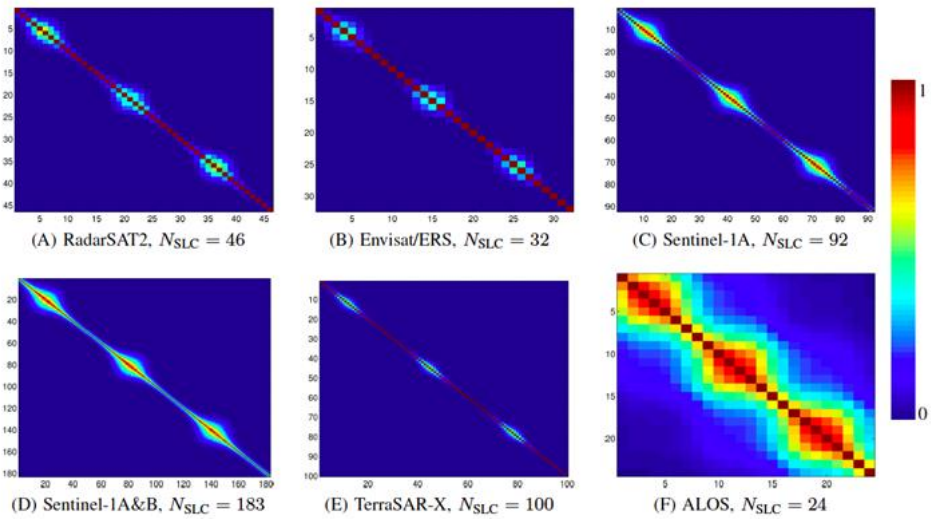

Figure 6. (A), (B), and (C) are three examples of coherence matrices in rural/pasture areas, corresponding to the locations P_A, P_B, and P_C in fig. 2. In the coherence matrices, the images are sorted based on the acquisition date (the months of acquisitions are indicated above the matrices). These matrices are the result of averaging coherence matrices of surrounding pixels. The average number of brothers and mean coherence of averaged pixels is indicated by $\bar{N}_{br}$ and $\bar{\gamma}$ respectively.

$$\gamma_T = \exp\left(\frac{-B_T}{\tau_1}\right) \exp\left(\frac{\cos(\omega(t_M+B_T-t_0)) - \cos(\omega(t_M-t_0))}{\omega\tau_2}\right), \quad (1)$$

where τ_1 and τ_2 are

$$\tau_1 = \frac{2}{\sigma_1^2}\left(\frac{\lambda}{4\pi}\right)^2 \text{ and } \tau_2 = \frac{2}{\sigma_2^2}\left(\frac{\lambda}{4\pi}\right)^2, \quad (\sigma_1^2 \geq \sigma_2^2,\ \tau_2 \geq \tau_1)$$

where $\omega = 2\pi/T$ is the angular frequency (with T=*1* year), t_0 is the initial time of the periodic signal, t_M is the master time, B_T is the temporal baseline, σ_1^2 is the variance factor which is constant in time, and σ_2^2 is the variance of the periodic component (the variance factors here are corresponding to the dispersion of the movement of elementary scatterers in a resolution cell). For the typical landscape of the case-study area (i.e., the white box in Figure 2 the three parameters of the model has been estimated in S. Samiei-Esfahany (2017) as: τ_1=13.5 days, τ_2=17 days, t_0=18th of March.

These parameters and the model of Eq. (1) are used in the next section for the feasibility study of exploitation of the corresponding DS-pixels for different satellite missions.

5. Feasibility Study

We used the estimated seasonal temporal-decorrelation for agricultural and pasture areas to simulate the corresponding coherence matrix for different satellite missions. In addition to the temporal decorrelation, other coherence components also are simulated. Table 1 shows the used parameters for each satellite. The simulated coherence matrices have been visualized in Figure 6. Note that the decorrelation rate components τ was estimated, in the previous section, only for the C-band data. For other bands these parameters can be simply computed as

$$\tau_{\text{X-band}} = \left(\frac{\lambda_X}{\lambda_C}\right)\tau_{C\text{-band}},\ \tau_{L\text{-band}} = \left(\frac{\lambda_L}{\lambda_C}\right)\tau_{C\text{-band}} \quad (2)$$

assuming that the elementary scatterers are the same for different wavelengths. The estimated τ_1 and τ_2 components are presented in the last two rows of Table 1 for different missions.

To assess the feasibility, we compute the Cramér-Rao Bound (CRB) of the phase time-series associated with the synthetic coherence matrices. The CRB is computed as proposed by Monti-Guarnieri and Tebaldini (2007) (see Appendix I for more information of CRB calculation). A CRB standard deviation (as here denoted by σ_{CRB}) should be interpreted as an indicator of the amount of information that exists in the data stack about the geometrical phase corresponding to each individual SAR image. A high σ_{CRB} (close to ~104°) means almost no information, and a low σ_{CRB} indicates that the information content is high. Note that, the CRB of the entire timeseries is an $N \times N$ matrix (assuming a stack of N number of images) whose diagonal elements provide the CRB variance (or standard deviation) an indicator that the information content of DS-pixels is sufficient to exploit their associated phase timeseries. As the max (σ_{CRB}) is dependent to the number of looks (L), we evaluated max (σ_{CRB}) for a number of looks L in the range of 20-400. The results are shown in Figure 7 for different satellite missions. The standard deviation of typical PS-pixels 25°), and the maximum possible standard deviation (104°) are also plotted. Note the logarithmic scaling of the computed max (σ_{CRB}) parameters for each phase in the time series. In order to reduce the all CRB standard deviations into a scalar metric, we compute the maximum of all the CRB standard deviations, denote by max(σ_{CRB}). The closeness of max(σ_{CRB}) to the expected standard deviation of typical PS-pixels (e.g., 25°) is used as we see that the CRB bound can possibly be larger than the maximum possible standard

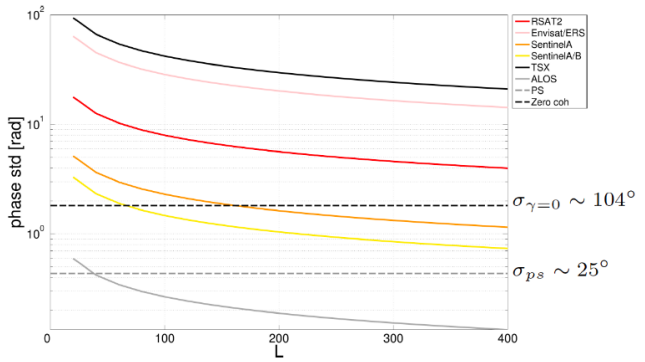

Figure 7. Predicted max(σ_{CRB}) for different multilooking factor *L* for different satellite missions in the case of six months data and for simulated coherence matricee Figure 6. The standard deviation of typical PS-pixels (25º), and the maximum possible standard deviation (104º$) are also plotted. Note the logarithmic scaling of y-axis.

deviation of 104º. For interpretation, we should consider the CRB bound as the inverse of the Fisher information content. Unlike the phase standard deviation (or variance) that has the upper bound of 104º, the CRB bound (or its inverse, the Fisher information) can be between zero to infinity by definition. In fact, a zero coherence phase has standard deviation of 104º, while it has no information and consequently its CRB bound is infinity. For high information, the square root of the CRB bound approaches to the expected standard deviation. The results show that, except for the L-band ALOS mission, none of the other sensors can provide sufficient information for the exploitation of DS-pixels with the assumed coherence behavior. Although different coherence components are simulated, the main driving mechanism behind the observed pattern in these results is the temporal decorrelation, which is mainly affected by the repeat time interval. For example, between Sentinel-1A case and the Sentinel-1A/B combination, the only difference is the repeat interval (i.e., 12 and 6 days, respectively), resulting in a better performance of Sentinel-1A/B. Based on these results we conclude that the information content of DS-pixels in three years datasets from these missions (except ALOS) is not enough for a successful utilization of these kinds of DS pixels, at least upto an L-factor of 400, which is already very large. Note that, in theory, if we continue to increase the L-factor, at some point we will approach to the quality of typical persistent scatterers and even better. However, for large multilooking factor we require a valid assumption of ergodicity over extremely large areas, which is not practical in real cases.

The results of Figure 7 are an indication of the information content of DS-pixels within the entire phase timeseries of three years. One would ask what would happen if we only process the coherent seasons (in this case winters). By processing the individual winter periods, it may be possible to use these kinds of DS-pixels. To assess this possibility, we repeat the experiment but, this time, using only 6 months of data during the winter period. The corresponding coherence matrices are shown in Figure 8, and the evaluated max(σ_{CRB}) parameters are presented in Figure 9. These results show a quite promising capability of Sentinel-1 data, which reach to the desired quality (i.e., σ_{ps}) with an L-factor of approximately 100 or higher (approximately 100 × 100 m), which is practical in real scenarios. For TSX data, the information content is still very poor. For other C-band data, i.e., RadarSAT2, Envisat, and ERS, the phase quality is still not sufficient if we only process six months of data during the high coherence season.

Table 1. Parameters used in the synthetic feasibility study for different radar satellite missions.

	Satellite Wavelength [mm]	**R2** 56	**Env/ERS** 56	**SenA** 56	**SenA/B** 56	**TSX** 31	**ALOS** 236
Constant components $\gamma_{thermal} = \frac{1}{1+SNR^{-1}}$	SNR [db]	12	12	12	12	12	12
$\gamma_{procc} = \text{sinc}^2(\sigma_{coreg,a,r})$	$\sigma_{coreg,az,ra}$ [pixel]	0.1	0.1	0.1	0.1	0.1	0.1
Geometrical dec. $\gamma_{geom} = \max(1 - \frac{\lvert B_\perp \rvert}{B_{\perp max}}, 0)$	$\sigma_{B_\perp}$ [m] $B_{\perp max}$ [km]	200 1.3	200 1.1	50 1.2	50 1.2	50 3.8	100 7.0
Temporal dec. eq.(1)	Repeat interval [days]	24	35	12	6	11	46
	$\hat{\tau}_1$ [days] $\hat{\tau}_2$ [days] $\hat{t}_0$ (date)	13.5 17 18Mar	13.5 17 18Mar	13.5 17 18Mar	13.5 17 18Mar	4.1 5.2 18Mar	239 301 18Mar

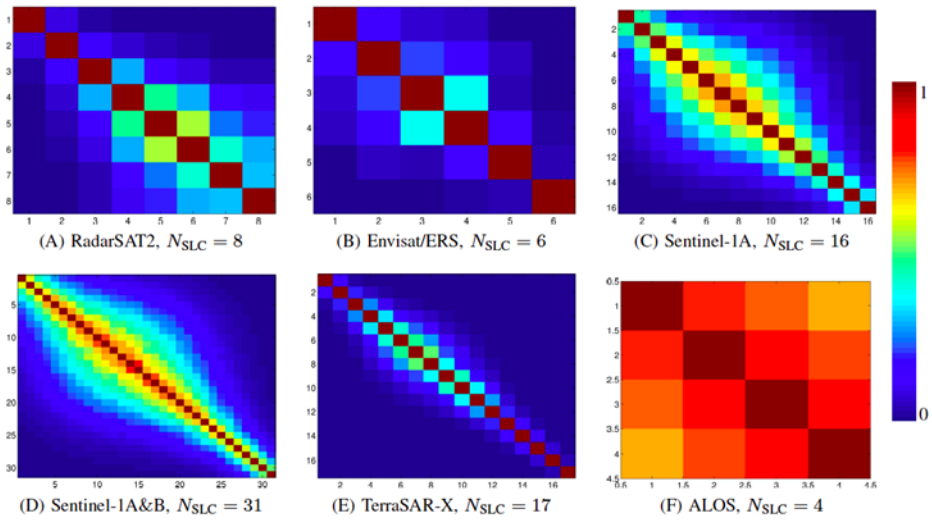

Figure 8. (A), (B), and (C) Predicted coherence matrices for studying the feasibility of DS exploitation for different radar satellite missions over agricultural and pasture areas, based on the estimated and assumed model parameters in table 1. Six months of data are assumed, resulting in a different number of images for each mission (due to their different repeat interval).

It should also be noted that, in addition to a sufficient phase quality, the number of images is also an important factor for a final feasibility study. By limiting the period of the full stack, we in fact reduce the number of final interferograms significantly. For example, for Envisat/ERS/RadarSAT2, over six months we get less than 10 images, which are too, low for standard timeseries processing. However the Sentinel-1 datasets have enough images for proper time-series processing even over six months. In summary, the high revisit time of Sentinel-1 data shows a promising expectation regarding DS exploitation by C-band data over agricultural and pasture areas. The X-band data have a limited potential over these kinds of landscapes, and L-band ALOS data have very good performance, however with limitations of a lower resolution and a long repeat interval.

6. Conclusions

In this study, the decorrelation pattern of typical DS-pixels in the Veendam case study have been used to simulate synthetic coherence matrices associated with the pasture areas in the region. The simulated coherence matrices are used to assess the feasibility of exploitation of DS-pixels in pasture areas for different satellite missions. The results show that, assuming an example of three-year stack of data, the information content in DS-pixels from current C-band and X-band missions is not enough for the successful utilization of their entire time-series. However by using intermittent series, e.g., by processing individual coherent periods, the results indicate that distributed scatterers can be exploited. Based on the proposed decorrelation model, the short repeat times of Sentinel-1 (6 or 12 days) results in a sufficient number of coherent interferograms over each winter period, enabling DS exploitation even over agricultural and pasture areas.

In this study, we only studied the exploitation of DS-pixels that show a good phase stability over the entire timeseries. However, over agricultural areas, as tillage and harvesting are known to destroy coherence completely, this approach is sub-optimal. The observed seasonal coherence behavior over agricultural areas shows the potential of extracting information from subsets of interferograms (for example subsets in the coherent seasons). In this regard, the potential of exploiting temporally coherent targets needs to be studied (e.g., see Ferretti et al., (2012)).

Furthermore, the focus in this study, and also in most of the other existing DS algorithms, is to process single-track data acquired from an individual satellite mission. However, recent research demonstrates the potential of joint processing of data stemming from different sensors to better estimate small deformation signals in pasture areas (Morishita & Hanssen, 2015). The feasibility of this kind of multi-sensor estimation over different landscapes should be assessed.

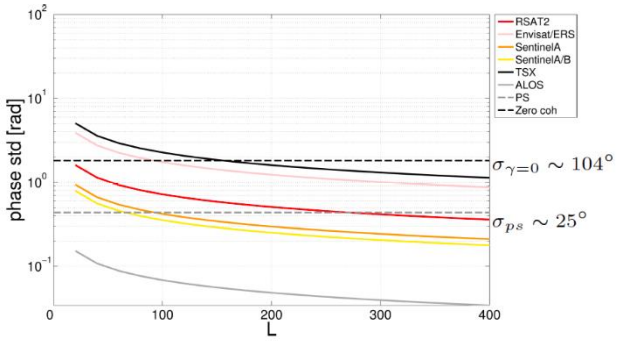

Figure 9. Predicted max($\boldsymbol{\sigma_{CRB}}$) for different multilooking factor L for different satellite missions in the case of six months data and for simulated coherence matrices of figure 8. The standard deviation of typical PS-pixels (25º), and the maximum possible standard deviation (104º$) are also plotted. Note the logarithmic scaling of y-axis

Appendix A: Cramér-Rao Bound for SAR Stacks

Monti-Guarnieri and Tebaldini (2007, 2008) have proposed a generic formulation for the evaluation of the lower Cramér-Rao bound (CRB) of the covariance matrix for the InSAR phase time-series. This CRB evaluates the highest achievable precision (or the lowest variance) for single-master phase estimators given a stack of SAR values for a pixel with a particular absolute coherence matrix, independent of the applied algorithm for the estimation. Given the $N \times N$ absolute coherence matrix Υ, the CRB is evaluated as (Monti-Guarnieri & Tebaldini, 2007) $Q_{\hat{b}} \geq (\Theta^T X \Theta)^{-1}$, where the inequality ($\geq$) indicates that the difference between the left and the right side of the inequality should be a non-negative definite matrix, and the matrices Θ and X are defined as follows:

- the matrix $\Theta = [0 \;\; I_{N-1}]^T$ is the $N \times (N-1)$ Jacobian matrix of the first-order partial derivative of SLC phases with respect to the unknown parameters, and
- the matrix X is the Fisher Information Matrix (FIM) associated with the estimates and is defined as $X = 2L(\Upsilon \circ \Upsilon^{-1} - I_N)$ where $\circ$ means the entry-wise product, L is the number of looks, and I_N is a $N \times N$ identity matrix.

Note that for the specific case of having only one interferogram constructed from two SLC images (i.e., N=2), the CRB is reduced to $Q_{\hat{b},\{N=2\}} = \sigma^2_{\varphi_{12}} \geq \frac{1-|\gamma_{12}|^2}{2L|\gamma|_{12}}$, which has been already derived for single interferometric phases.

References

Adam, N., Worawattanamateekul, B. K. M. E. J., & Kircher, M. (2003). "The development of a scientific permanent scatterer system." ISPRS Workshop High Resolution Mapping from Space, Hannover, Germany, 2003. 2003. 6 pp.

Berardino, P., Fornaro, G., Lanari, R., & Sansosti, E. (2002). A new algorithm for surface deformation monitoring based on small baseline differential SAR interferograms. *IEEE Transactions on Geoscience and Remote Sensing*, *40*(11), 2375-2383.

Cao, N., Lee, H., & Jung, H. C. (2016). A phase-decomposition-based PSInSAR processing method. *IEEE Transactions on Geoscience and Remote Sensing*, *54*(2), 1074-1090.

Costantini, M., Falco, S., Malvarosa, F., Minati, F., & Trillo, F. (2009, July). Method of persistent scatterer pairs (PSP) and high resolution SAR interferometry. In *Geoscience and Remote Sensing Symposium, 2009 IEEE International, IGARSS 2009* (Vol. 3, pp. III-904). IEEE.

Ferretti, A, A Fumagalli, F Novali, A. Rucci, C Prati, & F Rocca. (2012). "DEM reconstruction with SqueeSAR." 2012 Tyrrhenian Workshop on Advances in Radar and Remote Sensing (TyWRRS). 2012. 198-201.

Ferretti, A., Fumagalli, A., Novali, F., Prati, C., Rocca, F., & Rucci, A. (2011). A new algorithm for processing interferometric data-stacks: SqueeSAR. *IEEE Transactions on Geoscience and Remote Sensing*, *49*(9), 3460-3470.

Ferreti, A., Prati, C., & Rocca, F. (2000). Nonlinear subsidence rate estimation using permanent scatterers in differential SAR interferometry. *IEEE Transactions on Geoscience and Remote Sensing*, *38*(5), 2202-2212.

Ferretti, A., Prati, C., & Rocca, F. (1999). Permanent scatterers in SAR interferometry. In *Geoscience and Remote Sensing Symposium, 1999. IGARSS'99 Proceedings. IEEE 1999 International* (Vol. 3, pp. 1528-1530). IEEE.

Fornaro, G., Verde, S., Reale, D., & Pauciullo, A. (2015). CAESAR: An approach based on covariance matrix decomposition to improve multibaseline–multitemporal interferometric SAR processing. *IEEE Transactions on Geoscience and Remote Sensing*, *53*(4), 2050-2065.

Hooper, A. (2008). A multi- temporal InSAR method incorporating both persistent scatterer and small baseline approaches. *Geophysical Research Letters*, *35*(16).

Hooper, A., Zebker, H., Segall, P., & Kampes, B. (2004). A new method for measuring deformation on volcanoes and other natural terrains using InSAR persistent scatterers. *Geophysical research letters*, *31*(23).

Jiang, M., Ding, X., & Li, Z. (2014). Hybrid Approach for Unbiased Coherence Estimation for Multitemporal InSAR. *IEEE Trans. Geoscience and Remote Sensing*, *52*(5), 2459-2473.

Kampes, B. M. (2005). *Displacement parameter estimation using permanent scatterer interferometry* (Doctoral dissertation, TU Delft, Delft University of Technology).

Lanari, R., Mora, O., Manunta, M., Mallorqui, J. J., Berardino, P., & Sansosti, E. (2004). A small-baseline approach for investigating deformations on full-resolution differential SAR interferograms. *IEEE Transactions on Geoscience and Remote Sensing*, *42*(7), 1377-1386.

Lyons, S., & Sandwell, D. (2003). Fault creep along the southern San Andreas from interferometric synthetic aperture radar, permanent scatterers, and stacking. *Journal of Geophysical Research: Solid Earth*, *108*(B1).

Mahapatra, P., van der Marel, H., Hanssen, R., Holley, R., Samiei-Esfahany, S., Komac, M., & Fromberg, A. (2012, July). Radar transponders and their combination with GNSS for deformation monitoring. In *Geoscience and Remote Sensing Symposium (IGARSS), 2012 IEEE International* (pp. 3891-3894). IEEE.

Mahapatra, P., van der Marel, H., van Leijen, F., Samiei-Esfahany, S., Klees, R., & Hanssen, R. (2018). InSAR datum connection using GNSS-augmented radar transponders. *Journal of Geodesy*, *92*(1), 21-32.

Mahapatra, P., van der Marel, H., van Leijen, F., Samiei-Esfahany, S., Klees, R., & Hanssen, R. (2018). InSAR datum connection using GNSS-augmented radar transponders. *Journal of Geodesy*, *92*(1), 21-32.

Mahapatra, P., Samiei-Esfahany, S., & Hanssen, R. (2014, July). Geodetic network design for InSAR using reflectors and transponders. In *Geoscience and Remote*

Sensing Symposium (IGARSS), 2014 IEEE International (pp. 974-977). IEEE.

Mahapatra, P. S., Samiei- Esfahany, S., & Hanssen, R. F. (2015). Geodetic network design for InSAR. *IEEE Transactions on Geoscience and Remote Sensing*, *53*(7), 3669-3680.

Mahapatra, P. S., Samiei-Esfahany, S., van der Marel, H., & Hanssen, R. F. (2014). On the use of transponders as coherent radar targets for SAR interferometry. *IEEE Transactions on Geoscience and Remote Sensing*, *52*(3), 1869-1878.

Mahapatra, P. S., Samiei-Esfahany, S., Hanssen, R. F., & van der Marel, H. (2013, July). Geodetic quality assessment of a low-cost InSAR transponder. In *Geoscience and Remote Sensing Symposium (IGARSS), 2013 IEEE International* (pp. 1103-1106). IEEE.

Guarnieri, A. M., & Tebaldini, S. (2007). Hybrid Cramér–Rao bounds for crustal displacement field estimators in SAR interferometry. *IEEE signal processing letters*, *14*(12), 1012-1015.

Guarnieri, A. M., & Tebaldini, S. (2008). On the exploitation of target statistics for SAR interferometry applications. *IEEE Transactions on Geoscience and Remote Sensing*, *46*(11), 3436-3443.

Morishita, Y., & Hanssen, R. F. (2015). Deformation parameter estimation in low coherence areas using a multisatellite InSAR approach. *IEEE Transactions on Geoscience and Remote Sensing*, *53*(8), 4275-4283.

Morishita, Y., & Hanssen, R. F. (2015). Temporal decorrelation in L-, C-, and X-band satellite radar interferometry for pasture on drained peat soils. *IEEE Transactions on Geoscience and Remote Sensing*, *53*(2), 1096-1104.

Pepe, A., Yang, Y., Manzo, M., & Lanari, R. (2015). Improved EMCF-SBAS processing chain based on advanced techniques for the noise-filtering and selection of small baseline multi-look DInSAR interferograms. *IEEE Transactions on Geoscience and Remote Sensing*, *53*(8), 4394-4417.

Samiei Esfahany, S. (2017). Exploitation of distributed scatterers in synthetic aperture radar interferometry. PhD Thesis, Delft University of Technology, Delft, the Netherlands.

Samiei-Esfahany, S., Martins, J. E., van Leijen, F., & Hanssen, R. F. (2016). Phase estimation for distributed scatterers in InSAR stacks using integer least squares estimation. *IEEE Transactions on Geoscience and Remote Sensing*, *54*(10), 5671-5687.

Samiei-Esfahany, S., & Hanssen, R. F. (2013, July). New algorithm for InSAR stack phase triangulation using integer least squares estimation. In *Geoscience and Remote Sensing Symposium (IGARSS), 2013 IEEE International* (pp. 884-887). IEEE.

Samiei-Esfahany, S., Martins, J. E., van Leijen, F., & Hanssen, R. F. (2016). Phase estimation for distributed scatterers in InSAR stacks using integer least squares estimation. *IEEE Transactions on Geoscience and Remote Sensing*, *54*(10), 5671-5687.

Sandwell, D. T., & Price, E. J. (1998). Phase gradient approach to stacking interferograms. *Journal of Geophysical Research: Solid Earth*, *103*(B12), 30183-30204.

Schmidt, D. A., & Bürgmann, R. (2003). Time- dependent land uplift and subsidence in the Santa Clara valley, California, from a large interferometric synthetic aperture radar data set. *Journal of Geophysical Research: Solid Earth*, *108*(B9).

Van der Kooij, M. (2003, December). Coherent target analysis. In *Proceedings of the third International Workshop on ERS SAR Interferometry (FRINGE 2003), Frascati (Italy)* (pp. 2-5).

Van Leijen, F. J. (2014). *Persistent Scatterer Interferometry based on geodetic estimation theory* (Doctoral dissertation, TU Delft, Delft University of Technology).

Werner, C., Wegmuller, U., Strozzi, T., & Wiesmann, A. (2003, July). Interferometric point target analysis for deformation mapping. In *Geoscience and Remote Sensing Symposium, 2003. IGARSS'03. Proceedings. 2003 IEEE International* (Vol. 7, pp. 4362-4364). IEEE.

Wright, T., Parsons, B., & Fielding, E. (2001). Measurement of interseismic strain accumulation across the North Anatolian Fault by satellite radar interferometry. *Geophysical Research Letters*, *28*(10), 2117-2120.